PCCP



PAPER

View Article Online



Cite this: Phys. Chem. Chem. Phys., 2020, 22, 25264

X-ray photoelectron spectroscopy (XPS), ultraviolet photoelectron spectroscopy (UPS), atomic force

C8-BTBT on HOPG

Dongmei Niu, Han Huang and Yongli Gaoc

Modification of an ultrathin C₆₀ interlayer on the

Yuan Zhao, Da Xiaoliang Liu, *b Lin Li, C Shitan Wang, Youzhen Li, Haipeng Xie, A

electronic structure and molecular packing of

microscopy (AFM) and X-ray diffraction (XRD) were applied to investigate the electronic structure and molecular packing of C8-BTBT on HOPG with an ultrathin C60 interlayer. It was found that C8-BTBT displays a Vollmer-Weber (V-W) growth mode on HOPG, with an ultrathin C₆₀ interlayer (0.7 nm). Compared to the uniform lying-down growth mode as directly grown on HOPG, the C8-BTBT molecules here adopt a lying-down orientation at low coverage with some small tilt angles because the $\pi-\pi$ interaction between C8-BTBT and HOPG is partly disturbed by the C60 interlayer, delivering a higher highest occupied molecular orbital (HOMO) in C8-BTBT. An interface dipole of 0.14 eV is observed due to electron transport from C8-BTBT to C₆₀. The upward and downward band bending in C8-BTBT and C_{60} , respectively, near the C8-BTBT/ C_{60} interface reduces the hole transport barrier at the interface, facilitating the hole injection from C₆₀ to C8-BTBT, while a large electron transfer barrier from C₆₀ to C8-BTBT is detected at this interface, which effectively limits electron injection from C₆₀ to C8-BTBT. The HOMO of C8-BTBT near the interface is largely lifted up by the C_{60} insertion layer, which causes a p-doping effect and increases the hole mobility in C8-BTBT. Furthermore, owing to the lowest occupied molecular orbital (LUMO) of C_{60} residing in the gap of C8-BTBT, charge transfer occurs between C_{60} and the trap states in C8-BTBT to effectively passivate the trapping states. Our efforts aid a better understanding of the electron structure and film growth of anisotropic molecules and provide a useful strategy to improve the performance of C8-BTBT-based devices.

Received 12th August 2020, Accepted 11th October 2020

DOI: 10.1039/d0cp04288a

rsc.li/pccp

1. Introduction

In the past few decades, organic semiconductors (OSCs) have attracted considerable interests due to their particular characteristics compared to inorganic semiconductors. 1,2 Their potential applications in electronic devices include organic light-emitting diodes (OLEDs),^{3,4} organic field-effect transistors (OFETs),5-7 organic photovoltaic cells (OPVs)8,9 and organic spintronics. 10,11 Among various OSCs, as a derivative of the benzothieno[3,2-b]benzothiophene (BTBT) core structure, 2,7-diocty[1]benzothienol[3,2-b]benzothiophene (C8-BTBT) has been considered as a promising OSC in organic electronic devices, especially in OFETs, due to its excellent carrier

mobility, high air stability and easy synthesis. 12,13 As shown in the inset of Fig. 1, the intermolecular exchange of π -electrons of the BTBT core in the normal direction of self-assembled C8-BTBT contributes towards its high mobility. Mineawari et al. prepared C8-BTBT films with high crystallinity using inkjet

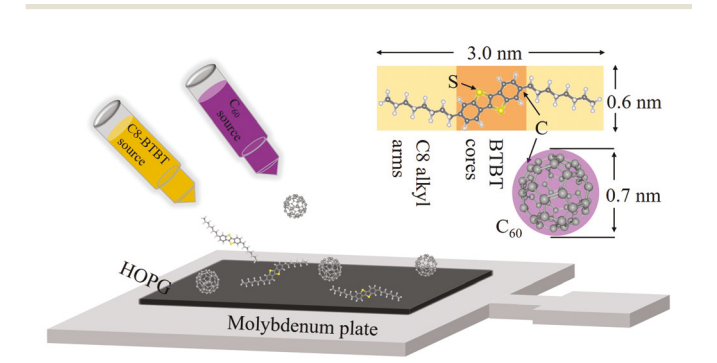


Fig. 1 Schematic diagram of the deposition of C_{60} and C8-BTBT molecules on HOPG, the upper right corner inset is the molecular structure of C8-BTBT and C₆₀.

^a School of Physics and Electronics, Central South University, Changsha, 410083,

^b School of Electronics and Information Engineering, Central South University of Forestry and Technology, Changsha, 410004, P. R. China. E-mail: xl liu@csu.edu.cn

^c Department of Physics and Astronomy, University of Rochester, Rochester,

printing, achieving a mobility of $16.4~\rm cm^2~V^{-1}~s^{-1}.^{14}~A$ recordbreaking mobility of up to $43~\rm cm^2~V^{-1}~s^{-1}$ reported by Yuan *et al.* in a C8-BTBT thin film transistor resulted in an upsurge in the exploration of C8-BTBT. So far, many efforts have been spent on exploring the applications of C8-BTBT. In work by He *et al.*, intrinsic hole mobility over $30~\rm cm^2~V^{-1}~s^{-1}$, band-like transport down to $150~\rm K$ and Ohmic contact with $100~\rm \Omega$ cm was demonstrated in an ultimate C8-BTBT monolayer based OTFT. By structuring a heterojunction based on a CH₃NH₃PbI₃/C8-BTBT interface, Tong *et al.* fabricated photodetectors with a photocurrent to dark current ratio of as high as $2.4~\rm \times~10^4$ and a fast response of around $4.0~\rm ms.^{17}$ Owing to the coexistence of an ultra-long spin lifetime and band-like transport in a BTBT-based single crystal, a micrometer-scale spin diffusion length was reported by Tsurumi *et al.* 18

As one of the key factors in achieving better device performance, the charge transport capability strongly depends on high quality OSC films that have few defects and traps. 19,20 Considering the structural anisotropy of C8-BTBT that is derived from its special structure, i.e., two insulating long alkyl groups along the axis direction of the BTBT cores and weak van der Waals (vDW) interactions, the electronic structure and molecular packing of C8-BTBT is easily affected by the underlying substrates. He et al. fabricated high-quality few-layer C8-BTBT molecular crystals grown on graphene or boron nitride (BN) substrates via vDW epitaxy. It was found that C8-BTBT adopted a lying-down phase at the initial stage but underwent a gradual transition to a free-standing phase as the thickness increased. OFETs based on a vertical C8-BTBT/ graphene heterostructure were confirmed to show excellent performance, while a high field-effect mobility of up to 10 cm² V⁻¹ s⁻¹ was obtained for C8-BTBT/BN-based OFETs.²¹ Such a phase transition was also observed in studies by Lyu et al. on C8-BTBT, 22,23 where C8-BTBT is prone to forming clusters with a disordered orientation on SiO2 substrate at low coverage of C8-BTBT due to the weak interaction between C8-BTBT and SiO₂. An unconventional downward band bending in C8-BTBT induced by the phase transition of C8-BTBT on HOPG or SiO₂ was also observed, which affects the charge transport in C8-BTBT and further affects the performance of C8-BTBT-based OFETs. All of the studies mentioned above provided an important clue for manipulating the carrier transport of anisotropic organic molecules similar to C8-BTBT and indicate the importance of the choice of substrates.

To improve the performance of C8-BTBT-based OFETs, many OSCs have been introduced to modify the energy level alignment and thus to facilitate charge transport at the interface 19,20,24,25 Modified using a F4-TCNQ layer, solution-crystallized OFETs based on C8-BTBT have been reported to deliver a high mobility (3.5–6 cm² V $^{-1}$ s $^{-1}$) and a low threshold voltage in air. 26 Paterson $et\ al.$ achieved a hole mobility of over 13 cm² V $^{-1}$ s $^{-1}$ by blending C8-BTBT and the conjugated polymer $\rm C_{16}IDT$ -BT. 27 Therefore, the influences of the functional OSC layer on the electronic structure and molecular packing of the C8-BTBT/OSC interface are also of importance and warrant further investigation. As an important acceptor

material, C_{60} has been extensively used to construct a P–N heterojunction with another OSC layer, functionally modifying the interfacial energy level alignment, passivating the trap states and even improving the thermal stability of some small organic molecules. ^{28–34}

In this paper, we studied the modification of the electronic structure and molecular packing of C8-BTBT on HOPG with an ML C_{60} interlayer using X-ray photoelectron spectroscopy (XPS), ultraviolet photoelectron spectroscopy (UPS), atomic force microscopy (AFM) and X-ray diffraction (XRD), amongst others. The effect of functionalizing the introduced C_{60} interlayers was also discussed and some interesting conclusions were drawn. Our work helps to understand the charge transport at the C8-BTBT/OSC interface and provide an idea of how to structure C8-BTBT-based OFETs that have high performance.

2. Experimental

Sample preparations and photoelectron spectroscopy (PES) were carried out in a multiple ultra-high vacuum chamber, which included a spectrometer chamber (base pressure <1 \times 10⁻¹⁰ mbar), an organic molecular beam chamber (base pressure $< 5 \times 10^{-9}$ mbar), a load lock chamber (base pressure <5 \times 10⁻⁸ mbar) and a radical distribution chamber (base pressure $< 5 \times 10^{-9}$ mbar) for interconnection. Freshly cleaved HOPG was degassed for 8 h at 450° in the spectrometer chamber. Shown in Fig. 2 are the XPS spectra of impurities related to the O 1s peaks, the UPS spectra and low energy electron diffraction (LEED) pattern of HOPG, which indicates a clean and high quality HOPG substrate. Prior to C8-BTBT deposition, an ultrathin C_{60} film of ~ 0.7 nm was thermally evaporated on HOPG by organic molecular beam epitaxy. It is worth mentioning that the thickness here obtained using a quartz crystal microbalance (QCM) is an average thickness based on film mass, which should be understood as a "nominal thickness" of C₆₀. Subsequently, a C8-BTBT layer with a final thickness of 6.4 nm was deposited layer by layer on the HOPG substrate in the same chamber. The deposition rate of C₆₀ and C8-BTBT was precisely controlled at 0.15 and 0.13 nm min⁻¹, respectively, which was monitored using a QCM. A schematic diagram of the deposition of C8-BTBT and C60 molecules is

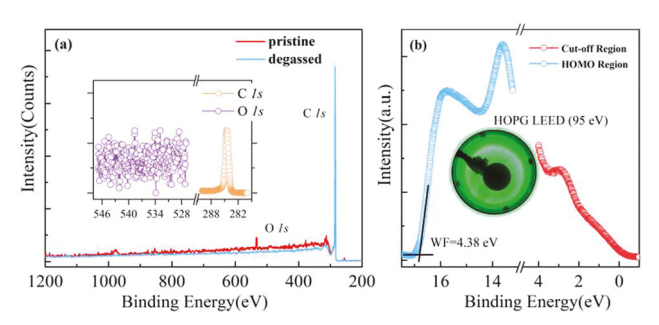


Fig. 2 (a) XPS full spectrum of pristine and degassed HOPG, in which the C 1s and O 1s core-level spectra of post-degassed HOPG are shown in the inset. (b) UPS spectra of post-degassed HOPG, in which the inset shows the LEED of HOPG.

shown in Fig. 1. The full details of this have been documented in our previous work.35-38

Thereafter, the XPS and UPS spectra of the prepared samples were collected *in situ* in the spectrometer chamber. For the XPS measurements, the X-ray source was operated at 100 W with a 40 eV pass energy and 100 meV step size. For the UPS measurements, the UV light spot diameter was about 1 mm and the energy resolution was about 70 meV, obtained from the Fermi edge of clean Au(111). The secondary cut-off edge was recorded with sample bias at -5 V. The angle between the incident photon and the emitted photoelectron direction was 45° for both XPS and UPS. The binding energies $(E_{\rm B})$ of all spectra were calibrated to the Fermi level $(E_{\rm F})$ of the energy analyzer. LEED images were acquired using a rear view four grid system (SPECS ErLEED 1000A). X-ray diffraction (Rigaku D. Max 2500 diffractometer, Cu K α radiation, $\lambda = 1.5418 \text{ Å}$) was utilized to identify the out-of-plane crystalline phases of the samples. Using silicon probes with a 10 nm curvature radius, AFM measurements were carried out in tapping mode for organic semiconductor film imaging.39,40 XRD and AFM measurements were performed in air. All the measurements were performed at room temperature.

3. Results and discussion

XPS spectra of C 1s and S 2p as a function of the C8-BTBT overlayer thickness are presented in Fig. 3, in which CasaXPS was used for the Gaussian fitting of the C 1s and S 2p curves. 41,42 For better visual comparison, all XPS and UPS spectra in Fig. 3 were normalized to unit intensity. The C 1s peak consists of three components associated with carbon from the HOPG substrate, C₆₀ interlayer and C8-BTBT, labeled as

C 1s (HOPG), C 1s (C₆₀) and C 1s (C8-BTBT), respectively. The XPS S 2p spectra of consist of two main peaks attributed to S 2p^{1/2} and S 2p^{3/2} with a fixed energy difference (1.18 eV), fixed ratio of intensity (2:1) and same full width at half maximum (FWHM, 1.52 eV). All peak positions are marked with vertical black short solid lines. As shown in Fig. 3a, there is almost no shift for C 1s (HOPG) with the initial deposition of 0.7 nm C₆₀ on HOPG and further deposition of up to 6.4 nm C8-BTBT on C₆₀/HOPG, while a distinguishable shift of about 0.08 eV toward a higher binding energy (BE) for C 1s (C₆₀) occurs with the 0.2 nm C8-BTBT deposition. Then, the C 1s (C_{60}) peak, as well as the C 1s (C8-BTBT) peak, moves toward a higher BE with an increase in C8-BTBT coverage, showing a total shift of 0.14 and 0.33 eV for C 1s (C_{60}) and C 1s (C8-BTBT), respectively, with a final deposition of 6.4 nm C8-BTBT. At this C8-BTBT overlayer thickness, the C 1s signals attributed to HOPG and C₆₀ are much too weak to be distinguished. As for the S 2p spectra shown in Fig. 3b, a similar shift toward a higher BE for C 1s (C8-BTBT) is also observed, showing a shift of 0.29 eV, slightly smaller than that of C 1s (C8-BTBT). Interestingly, the shift of C 1s (C_{60}) occurs just near the C8-BTBT/C₆₀ interface region, while the shift in C 1s (C8-BTBT) can be observed across the entire region.

Shown in Fig. 4a are the UPS spectra of the secondary electron cut-off edge, from which we can obtain the work function (WF) according to the formula WF = $h\nu - E_{\rm C}$, where $h\nu$ is the energy of incident photons and $E_{\rm C}$ is the BE of the cutoff onset. Linear extrapolation was adopted to determine the value of $E_{\rm C}$ as well as the highest occupied molecular orbital (HOMO), as reported in our previous work. 43 The WF of the post-processed bare HOPG substrate is 4.38 eV, and it shifts to 4.56 eV as 0.7 nm of C₆₀ is deposited on HOPG. Although there is a 0.18 eV difference in the WF between C₆₀ and HOPG, no

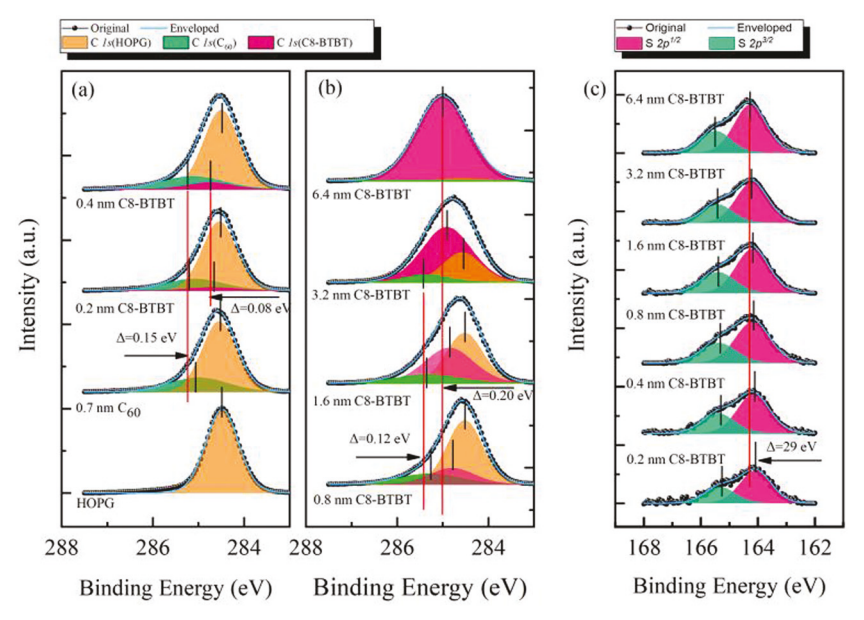


Fig. 3 Thickness dependence XPS core-level spectra of (a) and (b) C 1s and (c) S 2p in C8-BTBT, the C 1s peak is fitted to C 1s (HOPG), C 1s (C₆₀) and C 1s (C8-BTBT), the S 2p peak is fitted to S $2p^{1/2}$ and S $2p^{3/2}$.

PCCP Paper

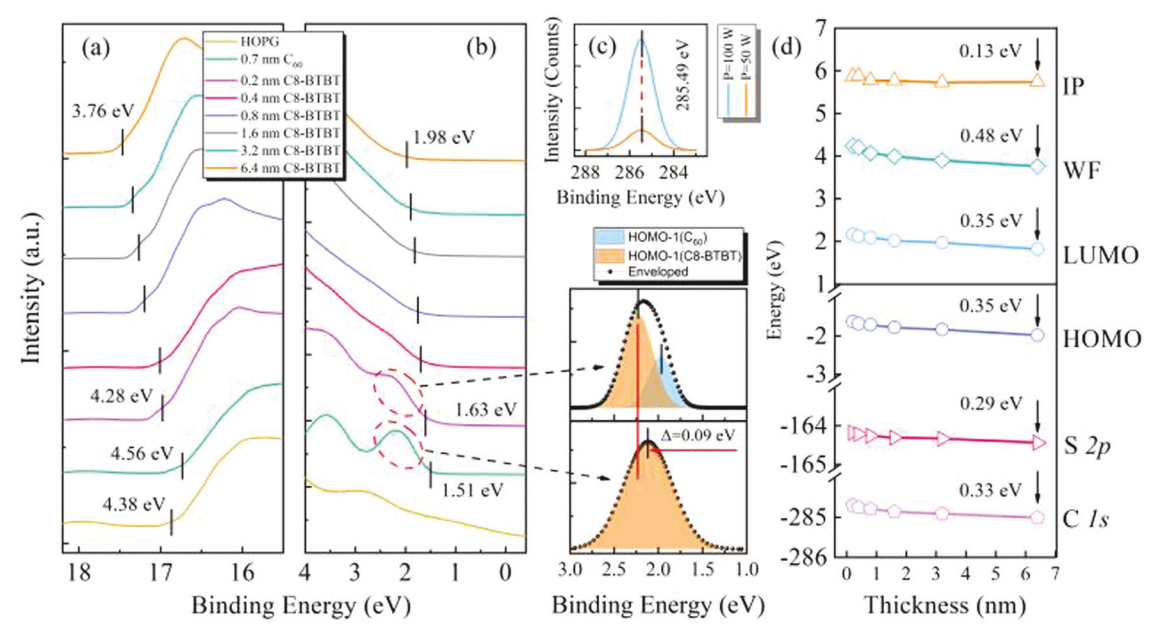


Fig. 4 Thickness dependent UPS spectra of the (a) cut-off and (b) HOMO regions; (c) upper panel: XPS core-level spectra of C 1s for 6.4 nm C8-BTBT/ 0.7 nm C_{60} /HOPG with an X-ray source modulated at 100 and 50 W, respectively, lower panel: the Gaussian fitting of HOMO with HOMO-1(C_{60}) and HOMO-1(C8-BTBT); (d) the evolution of S 2p, HOMO, WF and IP with increasing C8-BTBT coverage.

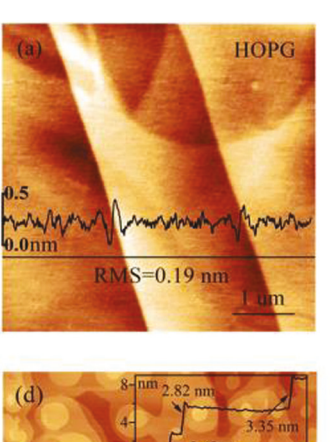
charge redistribution occurs at the C₆₀/HOPG interface, which is supported by the unchanged position of the C 1s (HOPG) peaks. Hereafter, the WF suddenly reduces to 4.28 eV with a deposition of 0.2 nm C8-BTBT on as-prepared 0.7 nm C₆₀/HOPG and then monotonically decreases with the further deposition of C8-BTBT. The WF eventually attenuates to 3.76 eV at 6.4 nm C8-BTBT, comparable to that of bulk-phase C8-BTBT.²²

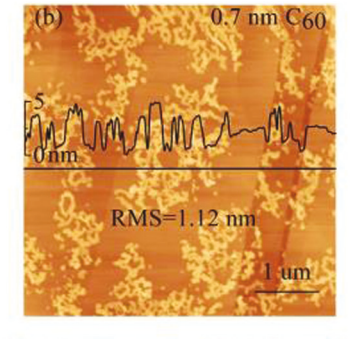
The evaporation thickness dependent HOMO values are presented in Fig. 4b. The HOMO is 1.51 eV upon the deposition of 0.7 nm C₆₀, and two distinct characteristic peaks derived from the C₆₀ valence band appear at 2.11 and 3.59 eV, named as HOMO−1 and HOMO−2 here, respectively. With the following deposition of C8-BTBT, the intensities of the two peaks decrease with an increase in FWHM due to the effect of the contribution from C8-BTBT. To distinguish between the contributions that C₆₀ and C8-BTBT make to the HOMO, the HOMO-1 peaks for 0.7 nm C₆₀/HOPG and 0.2 nm C8-BTBT/ 0.7 nm C₆₀/HOPG were fitted with HOMO-1(C₆₀) and HOMO-1(C8-BTBT) after subtracting the background, as shown in Fig. 3c (the lower panel). The HOMO-1(C₆₀) presents a slight shift of 0.09 eV toward a higher BE and the HOMO-1(C8-BTBT) was found to be responsible for the HOMO onset of the sample, which is determined at 1.63 eV. Upon further increasing the coverage of C8-BTBT, the HOMO onset shows the same shift trend as the cut-off edge, with a total shift of 0.35 eV. The HOMO-1(C₆₀) gradually disappears as the thickness of C8-BTBT increases. However, the HOMO-1(C8-BTBT) is also found to vanish at high coverage of C8-BTBT with the increasing thickness of C8-BTBT, which seems contradictory. In fact, the HOMO-1(C8-BTBT) peak is supposed to be associated with the lying-down phase of C8-BTBT and the gradual transition to its standing-up phase

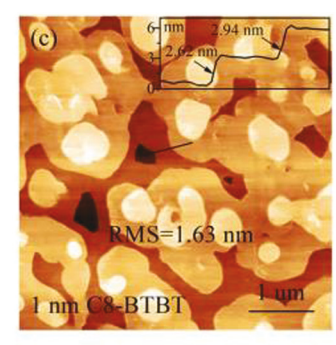
results in the disappearance of HOMO-1(C8-BTBT) as the coverage of C8-BTBT increases.44

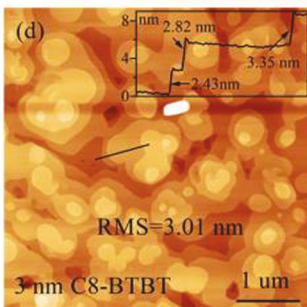
To acquire an intuitive picture of the change in all energy levels, the thickness dependent evolution of C 1s, S 2p, HOMO, low unoccupied molecular orbital (LUMO), WF and ionization potential (IP) of C8-BTBT are plotted in Fig. 4d. The band gap of C8-BTBT is taken as 3.84 eV. 45 It can be obviously observed that as the thickness of C8-BTBT increases, the C1s, S2p, HOMO and LUMO present an almost same downward shift of ~ 0.35 eV, while the WF shows a greater shift of around 0.48 eV, which leads to an IP decrease of ~ 0.13 eV. To ensure the observed energy level shifts toward a higher BE are exclusively ascribed to the nature of samples, charging effects need to be ruled out here, which are often observed in PES tests for many organic semiconductors that have poor conductivity. To this end, in Fig. 3c (the upper panel) we present the C 1s spectra of the 6.4 nm C8-BTBT/0.7 nm C₆₀/HOPG interface at different X-ray source power. If there is a charging effect in play in this sample, the excited photoelectron numbers should be dependent on the power of the X-ray source, which induces a different energy level shift toward a higher BE. Fortunately, the fact that the C 1s peak is nearly at the same position using both 50 and 100 W X-ray sources excludes the possibility of a charging effect, most likely due to the excellent conductivity of C8-BTBT. In fact, such an unconventional decrease in the IP may be ascribed to the phase transition of π -conjugated molecules with structural anisotropy, as reported in previous studies on C8-BTBT/HOPG(SiO2) and other cases involving 6T, DH6T and CuPc. 46,47 The interface dipole from the different oriented layer of C8-BTBT causes the band bending of C8-BTBT and the C-H surface dipole in the upper layer accounts for the decrease in IP. However, some interesting differences can be observed and remain unclear here

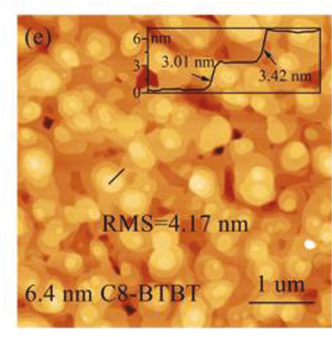
PCCP











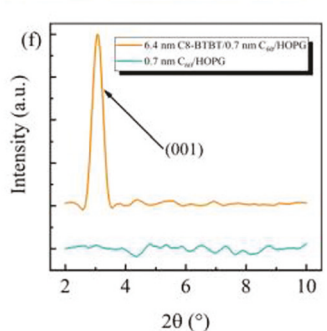


Fig. 5 AFM morphology images (5 μm × 5 μm) of the (a) HOPG, (b) 0.7 nm C₆₀ on HOPG, (c) 1 nm C8-BTBT, (d) 3 nm C8-BTBT, (e) 6.4 nm C8-BTBT on 0.7 nm C_{60} /HOPG, and (f) out-of-plane XRD spectra of the 0.7 nm C_{60} /HOPG and 6.4 nm C8-BTBT/0.7 nm C_{60} /HOPG interfaces.

owing to the additional insertion of 0.7 nm C₆₀ between C8-BTBT and HOPG. More efforts will be carried out to elucidate the electronic structure and the molecular packing mode of the C8-BTBT/0.7 nm C₆₀/HOPG interface.

To verify the molecular packing of C8-BTBT on 0.7 nm C₆₀/ HOPG, morphology images of HOPG, 0.7 nm C₆₀ and different coverages of C8-BTBT were characterized by AFM, as shown in Fig. 5a-e. The root mean square (RMS) of processed HOPG was measured to be as low as 0.19 nm, as shown in Fig. 5a, and the cross section along the black line shows a height variation of no more than 0.5 nm, indicating that a high quality HOPG substrate that is atomically smooth was obtained and may minimize the impacts of the substrate on the overlayers in our research. As a 0.7 nm C₆₀ layer is deposited on HOPG, many formed C₆₀ clusters are unevenly distributed on the HOPG substrate with considerable exposure of the underlying substrate. The average height of the clusters far exceeds 0.7 nm, as confirmed by the height distribution of C₆₀ along the line in Fig. 5b, so the 0.7 nm C₆₀/HOPG configuration delivers a relatively big RMS of 1.12 nm. As shown in the inset of Fig. 1, owing to the structural anisotropy of C8-BTBT, it is easy to examine the packing orientation of C8-BTBT molecules from AFM measurements. In Fig. 5c, with the deposition of 1 nm C8-BTBT, several layers of C8-BTBT form on the underlying layer with some large-size islands and an RMS of 1.63 nm. With the deposition of more C8-BTBT molecules, the separated islands gradually coalesce together and form new continuous layers, and new C8-BTBT islands form on the upper layer at the same time, from which we should infer that C8-BTBT molecules grow on 0.7 nm C₆₀/HOPG in a V-W growth mechanism, as shown in Fig. 5d and e.

From the cross section along the black line in Fig. 5c-e, the evolution of the layer height of C8-BTBTcan be observed. We

can clearly see that the terrace height of C8-BTBT increases with the increasing coverage of C8-BTBT with a step height of around 3.42 nm with the deposition of 6.4 nm C8-BTBT, which is identical to the height of the standing orientation C8-BTBT molecules. As expected, the C8-BTBT molecules eventually relax to a standing-up phase regardless of their initial phase, induced by the underlying substrate. The increasing layer height of C8-BTBT means that a phase transition in the orientation of the C8-BTBT molecules occurs during the relaxation process. However, the lowest height of the terrace measured here is 2.42 nm, which is much greater than the height of the C8-BTBT molecules that are completely lying-down. Therefore, the molecular packing of C8-BTBT on 0.7 nm C60/HOPG cannot be completely figured out here, especially for a low coverage of C8-BTBT molecules. Out-of-line XRD was also performed to characterize the crystallinity and crystal orientation of the C8-BTBT film, as shown in Fig. 5f. Compared to the pattern of the sample without deposition of C8-BTBT, a new peak at $\sim 3^{\circ}$ was observed for the 6.4 nm C8-BTBT/0.7 nm C₆₀/HOPG. The peak is assigned as the (001) Bragg reflection of C8-BTBT, with a d-spacing of around 3.02 nm. The strong reflection peak implies the high crystallinity of 6.4 nm C8-BTBT on 0.7 nm C₆₀/HOPG and indicates a highly ordered standing-up phase of C8-BTBT at this coverage.

The C8-BTBT thickness dependent intensity evolution of the XPS core-level spectra in the C8-BTBT layer and the underlying C₆₀ and HOPG layers in Fig. 6 provide further insight on the film growth mode of C8-BTBT on 0.7 nm C₆₀/HOPG. As reported in our previous work, the decreasing peak intensity of the elements in the substrate and the increasing peak intensity of those in the overlayer exponentially change with the overlayer thickness as the molecules are deposited on the substrate

PCCP Paper

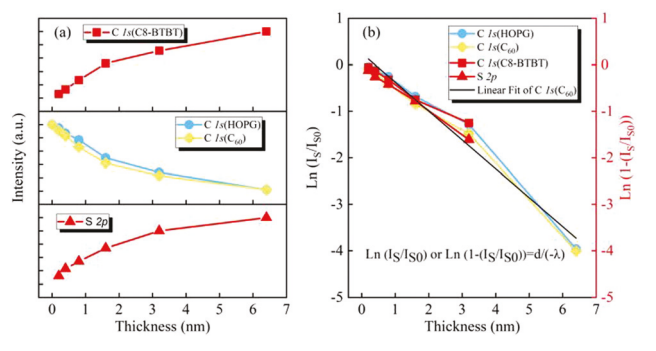


Fig. 6 (a) The intensity evolution of the C 1s and S 2p peaks with increasing C8-BTBT thickness, (b) the dependence of $ln(I_S/I_{S0})$ or ln $(1 - I_S/I_{SO})$ on the C8-BTBT thickness, where I_S and I_{SO} are the peak intensities with and without coverage of C8-BTBT molecules.

layer by layer, which can be described by the formulae I_S = $I_{S0}e^{-d/\lambda}$ and $I_S = I_{S0}(1 - e^{-d/\lambda})$, respectively, where λ is the mean free path (MFP) of the electron crossing the coverage layer and d is the thickness of the coverage. 48,49 It is apparent that the intensities of C 1s (HOPG) and C 1s (C₆₀), C 1s (C8-BTBT) and S 2p perfectly agree with the formulas above. To further analyze the intensity evolution, the normalized intensities as a function of thickness are plotted in Fig. 6b. The intensities of C 1s (HOPG) and C 1s (C₆₀) show a similar slope change. The linear fit of C 1s (C₆₀) is presented and an electron MFP of \sim 2.16 nm was achieved, which conforms to normal values among organic semiconductor materials. Interestingly, a slight increase in the absolute value of the C 1s (C₆₀) slope is observed upon increasing the C8-BTBT thickness, which may serve as further evidence of the V-W growth mode of C8-BTBT on the 0.7 nm C₆₀/HOPG substrate. The formation of C8-BTBT clusters at low coverage leaves a larger area of exposure of the underlying C₆₀ layer than an evenly distributed C8-BTBT film, so the photoelectron intensity associated with the C 1s (C₆₀) decreases gradually at first. Then, the coalescence of the C8-BTBT islands leaves less of the underlying C₆₀ layer exposed, leading to a quicker intensity attenuation of photoelectrons.

Based on the XPS and UPS data, a phase transition from the lying-down orientation to the standing-up orientation for the C8-BTBT molecules is inferred, but the molecular orientation

of C8-BTBT in the initial coverage stage remains unclear. Compared to C8-BTBT directly deposited on HOPG, we found that the HOMO value at low coverage of C8-BTBT for C8-BTBT deposited on 0.7 nm C₆₀/HOPG is apparently greater and the decrease in WF, HOMO, C 1s, S 2p and IP are much smaller, which probably means that the C8-BTBT molecules do not lie completely flat on HOPG at the initial stage because the π - π interaction between C8-BTBT and HOPG is not completely propagated by the ultrathin C₆₀ interlayer.²³ Further evidence was provided by AFM characterization. Shown in Fig. 7a is a schematic of the molecular packing of C8-BTBT on 0.7 nm $C_{60}/HOPG$. The step height of 2.42 nm in Fig. 5c indicates that the C8-BTBT molecules adopt a lying-down orientation with a big tilt-up angle at low C8-BTBT coverage. Compared to the case without the 0.7 nm C₆₀ interlayer, in which C8-BTBT molecules present an approximately complete lying-down orientation with some slight disorder, the big tilt-up angle here can be ascribed to the disordered effect derived from the C_{60} interlayer. The step height of 3.42 nm is associated with the standing-up orientation of the C8-BTBT molecules at high C8-BTBT coverage.

The energy level alignment of 6.4 nm C8-BTBT/0.7 nm C₆₀/ HOPG is presented in Fig. 7b, in which the $E_{\rm g}$ value of C_{60} is taken as 2.3 eV here. 50 Owing to the negligible difference in the WF between C₆₀ and HOPG, no charge transport occurs and no dipole forms at the 0.7 nm C₆₀/HOPG interface, hence band bending behavior is not observed at the C60 side near the interface. At the C8-BTBT/C60 interface, an interface dipole of 0.14 eV pointing from the C8-BTBT to C60 is observed due to electron transport from the C8-BTBT region to the C60 region as a result of the WF difference between C8-BTBT and C60. So, downward band bending in the C60 layer happens naturally near the interface. The WF of 0.7 nm C₆₀ measured here is much smaller than the bulk-phase C60, as detailed in our previous work, 31,51 most likely due to the contributions from the HOPG substrate considering the evenly distributed C60 on HOPG without complete coverage. 52,53 In terms of the C8-BTBT side, noticeable downward band bending is also observed, which induces a built-in field and thus a p-doped surface state region. Both the charge transfer at the C8-BTBT/C₆₀ interface and the orientation transition of C8-BTBT contribute to the downward band bending of C8-BTBT. However, the former

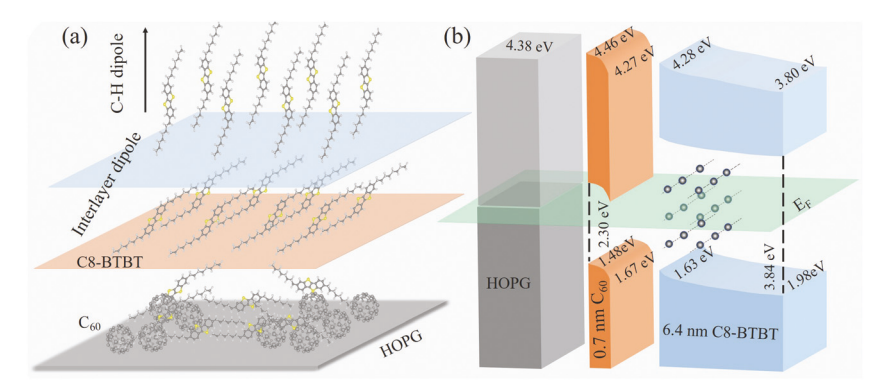


Fig. 7 Schematic drawing of the (a) molecular packing and (b) energy level alignment for C8-BTBT on 0.7 nm C₆₀/HOPG.

PCCP

always occurs very near to the interface, while the latter seems to occur farther away from the interface, as supported by the minor decrease in IP near the interface.

Strong hole accumulation near this interface may facilitate the formation of a high concentration conducting channel when this interface is incorporated into an organic device. In addition, combined with the band bending of C8-BTBT and C60, the difference in the HOMO between C8-BTBT and C60 is greatly reduced, which means a smaller hole barrier forms at the interface for hole transport from C8-BTBT to HOPG. At the same time, the difference in LUMO between C8-BTBT and C₆₀ increases at the very near interface region, which increases the electron barrier for electron transport from C₆₀ to C8-BTBT and reduces the possibility of electron-hole recombination at the interface. Finally, the LUMO of C₆₀ resides in the gap of C8-BTBT owing to the wide gap of C8-BTBT, and the trap states derived from the defects in C8-BTBT can be greatly passivated after the in-gap trap states above the level of the HOMO are filled, which can deliver a weak hysteresis effect and a small threshold voltage in related devices. Therefore, the insertion of 0.7 nm C₆₀ is expected to improve the performance of C8-BTBT-based devices with low threshold voltage and higher mobility. Our results show that the C8-BTBT films modified by ultrathin C₆₀ interlayer have great potential for use in the organic electronic device field.

4. Conclusions

In summary, the electronic structure and molecular packing mode of a C8-BTBT/0.7 nm C₆₀/HOPG interface have been investigated using XPS, UPS, AFM and XRD. C8-BTBT molecules grow on 0.7 nm $C_{60}/HOPG$ in a V-W mode and the π - π interaction between C8-BTBT and HOPG is weakened by the thin C₆₀ interlayer to some extent, which makes the C8-BTBT molecules still adopt a lying-down orientation at low coverage, but with a tilt angle. The tilt up C8-BTBT layer has a higher HOMO than the completely lying-down ones. Downward band bending occurs in both C8-BTBT and the C60 layer at the C8-BTBT/C60 interface due to carrier transfer together with the phase transition in C8-BTBT. The HOMO of C8-BTBT near the interface is largely lifted by the C₆₀ insertion layer, which causes a p-doping effect and an increase in hole mobility in C8-BTBT. The hole transfer barrier at the interface is largely reduced while electron transfer barrier is clearly increased. Owing to the wide gap of C8-BTBT, the LUMO of C₆₀ residing in the gap of C8-BTBT can probably passivate the trapping states in C8-BTBT. Our efforts help to better understand the electron structure and film growth of anisotropic molecules and provide a useful strategy to improve the performance of C8-BTBT-based devices.

Conflicts of interest

The authors declare that they have no known competing financial interests or personal relationships that could have appeared to influence the work reported in this paper.

Acknowledgements

This work was supported by the National Natural Science Foundation of China (Grant No. 51673217) and the Fundamental Research Funds for the Central South University (502221903). Y. Gao acknowledges the support of the National Science Foundation (Grant No. DMR-1903962).

References

- 1 J. Xu, H. C. Wu, C. Zhu, A. Ehrlich, L. Shaw, M. Nikolka, S. Wang, F. Molina-Lopez, X. Gu, S. Luo, D. Zhou, Y. H. Kim, G. N. Wang, K. Gu, V. R. Feig, S. Chen, Y. Kim, T. Katsumata, Y. Q. Zheng, H. Yan, J. W. Chung, J. Lopez, B. Murmann and Z. Bao, Nat. Mater., 2019, 18, 594-601.
- 2 S. E. Root, S. Savagatrup, A. D. Printz, D. Rodriquez and D. J. Lipomi, Chem. Rev., 2017, 117, 6467-6499.
- 3 T. Sekitani, H. Nakajima, H. Maeda, T. Fukushima, T. Aida, K. Hata and T. Someya, Nat. Mater., 2009, 8, 494-499.
- 4 S. T. Lee, Y. M. Wang, X. Y. Hou and C. W. Tang, Appl. Phys. Lett., 1999, 74, 670-672.
- 5 C. Zhang, P. Chen and W. Hu, Chem. Soc. Rev., 2015, 44, 2087-2107.
- 6 H. Sirringhaus, Adv. Mater., 2014, 26, 1319-1335.
- 7 J. W. Shi, H. B. Wang, D. Song, H. K. Tian, Y. H. Geng and D. H. Yan, Adv. Funct. Mater., 2007, 17, 397-400.
- 8 C. W. Tang, Appl. Phys. Lett., 1986, 48, 183-185.
- 9 J. Wang, S. Luo, Y. Lin, Y. Chen, Y. Deng, Z. Li, K. Meng, G. Chen, T. Huang, S. Xiao, H. Huang, C. Zhou, L. Ding, J. He, J. Huang and Y. Yuan, Nat. Commun., 2020, 11, 582.
- 10 C. Barraud, P. Seneor, R. Mattana, S. Fusil, K. Bouzehouane, C. Deranlot, P. Graziosi, L. Hueso, I. Bergenti, V. Dediu, F. Petroff and A. Fert, Nat. Phys., 2010, 6, 615-620.
- 11 M. Cinchetti, V. A. Dediu and L. E. Hueso, Nat. Mater., 2017, 16, 507-515.
- 12 H. Ebata, T. Izawa, E. Miyazaki, K. Takamiya, M. Ikeda, H. Kuwabara and T. Yui, J. Am. Chem. Soc., 2007, 129, 15732-15733.
- 13 Y. Tsutsui, G. Schweicher, B. Chattopadhyay, T. Sakurai, J. B. Arlin, C. Ruzie, A. Aliev, A. Ciesielski, S. Colella, A. R. Kennedy, V. Lemaur, Y. Olivier, R. Hadji, Sanguinet, F. Castet, S. Osella, D. Dudenko, D. Beljonne, J. Cornil, P. Samori, S. Seki and Y. H. Geerts, Adv. Mater., 2016, 28, 7106-7114.
- 14 H. Minemawari, T. Yamada, H. Matsui, J. Tsutsumi, S. Haas, R. Chiba, R. Kumai and T. Hasegawa, Nature, 2011, 475,
- 15 Y. Yuan, G. Giri, A. L. Ayzner, A. P. Zoombelt, S. C. Mannsfeld, J. Chen, D. Nordlund, M. F. Toney, J. Huang and Z. Bao, Nat. Commun., 2014, 5, 3005.
- 16 D. He, J. Qiao, L. Zhang, J. Wang, J. Xu, W. Ji and X. Wang, Sci. Adv., 2017, 3, 1-9.
- 17 S. Tong, J. Sun, C. Wang, Y. Huang, C. Zhang, J. Shen, H. Xie, D. Niu, S. Xiao, Y. Yuan, J. He, J. Yang and Y. Gao, Adv. Electron. Mater., 2017, 3, 1700058.

- 18 J. Tsurumi, H. Matsui, T. Kubo, R. Häusermann, C. Mitsui, T. Okamoto, S. Watanabe and J. Takeya, Nat. Phys., 2017, 13, 994-998.
- 19 K. Zhang, N. B. Kotadiya, X. Y. Wang, G. J. A. H. Wetzelaer, T. Marszalek, W. Pisula and P. W. M. Blom, Adv. Electron. Mater., 2020, 6, 1901352-1901357.
- 20 N. Koch, ChemPhysChem, 2007, 8, 1438-1455.
- 21 D. He, Y. Zhang, Q. Wu, R. Xu, H. Nan, J. Liu, J. Yao, Z. Wang, S. Yuan, Y. Li, Y. Shi, J. Wang, Z. Ni, L. He, F. Miao, F. Song, H. Xu, K. Watanabe, T. Taniguchi, J. B. Xu and X. Wang, Nat. Commun., 2014, 5, 5162.
- 22 L. Lyu, D. Niu, H. Xie, Y. Zhao, N. Cao, H. Zhang, Y. Zhang, P. Liu and Y. Gao, Phys. Chem. Chem. Phys., 2017, 19, 1669-1676.
- 23 L. Lyu, D. Niu, H. Xie, N. Cao, H. Zhang, Y. Zhang, P. Liu and Y. Gao, I. Chem. Phys., 2016, 144, 034701.
- 24 S. Lach, A. Altenhof, K. Tarafder, F. Schmitt, M. E. Ali, M. Vogel, J. Sauther, P. M. Oppeneer and C. Ziegler, Adv. Funct. Mater., 2012, 22, 989-997.
- 25 X. Liu, Q. Han, Y. Liu, C. Xie, C. Yang, D. Niu, Y. Li, H. Wang, L. Xia, Y. Yuan and Y. Gao, Appl. Phys. Lett., 2020, 116, 253303.
- 26 J. Soeda, Y. Hirose, M. Yamagishi, A. Nakao, T. Uemura, K. Nakayama, M. Uno, Y. Nakazawa, K. Takimiya and J. Takeya, Adv. Mater., 2011, 23, 3309-3314.
- 27 A. F. Paterson, N. D. Treat, W. Zhang, Z. Fei, G. Wyatt-Moon, H. Faber, G. Vourlias, P. A. Patsalas, O. Solomeshch, N. Tessler, M. Heeney and T. D. Anthopoulos, Adv. Mater., 2016, 28, 7791-7798.
- 28 C. Fan, A. P. Zoombelt, H. Jiang, W. Fu, J. Wu, W. Yuan, Y. Wang, H. Li, H. Chen and Z. Bao, Adv. Mater., 2013, 25, 5762-5766.
- 29 T. D. Ibragimov, A. R. Imamaliyev and G. F. Ganizade, Mol. Cryst. Liq. Cryst., 2019, 691, 27-34.
- 30 H. Li, C. Fan, W. Fu, H. L. Xin and H. Chen, Angew. Chem., Int. Ed., 2015, 54, 956-960.
- 31 X. Liu, C. Wang, C. Wang, I. Irfan and Y. Gao, Org. Electron., 2015, 17, 325-333.
- 32 S. Olthof, S. Singh, S. K. Mohapatra, S. Barlow, S. R. Marder, B. Kippelen and A. Kahn, Appl. Phys. Lett., 2012, 101, 253303.
- 33 X. H. Zhang and B. Kippelen, Appl. Phys. Lett., 2008, 93, 133305.
- 34 X. Liu, S. Yi, C. Wang, C. Wang and Y. Gao, J. Appl. Phys., 2014, 115, 163708.
- 35 P. Liu, X. Liu, L. Lyu, H. Xie, H. Zhang, D. Niu, H. Huang, C. Bi, Z. Xiao, J. Huang and Y. Gao, Appl. Phys. Lett., 2015, 106, 193903.

- 36 Y. Liu, C. Xie, W. Tan, X. Liu, Y. Yuan, Q. Xie, Y. Li and Y. Gao, Org. Electron., 2019, 71, 123-130.
- 37 W. Tan, C. Xie, Y. Liu, Y. Zhao, L. Li, X. Liu, Y. Yuan, Y. Li and Y. Gao, Synth. Met., 2018, 246, 101-107.
- 38 Y. Zhao, X. Liu, L. Lyu, L. Li, W. Tan, S. Wang, C. Wang, D. Niu, H. Xie, H. Huang and Y. Gao, Synth. Met., 2017, 229, 1-6.
- 39 Y. Huang, J. Sun, J. Zhang, S. Wang, H. Huang, J. Zhang, D. Yan and Y. Gao, Org. Electron., 2016, 36, 73.
- 40 S. Wang, L. Lyu, D. Niu, L. Zhang, H. Huang and Y. Gao, Appl. Phys. Lett., 2019, 114, 241602.
- 41 L. Li, C. Wang, C. Wang, S. Tong, Y. Zhao, H. Xia, J. Shi, J. Shen, H. Xie, X. Liu, D. Niu, J. Yang, H. Huang, S. Xiao, J. He and Y. Gao, Org. Electron., 2019, 65, 162-169.
- 42 H. Xie, D. Niu, L. Lyu, H. Zhang, Y. Zhang, P. Liu, P. Wang, D. Wu and Y. Gao, Appl. Phys. Lett., 2016, 108, 034701.
- 43 X. Liu, C. Wang, I. Irfan, S. Yi and Y. Gao, Org. Electron., 2014, 15, 977-983.
- 44 S. Wang, D. Niu, L. Lyu, Y. Huang, X. Wei, C. Wang, H. Xie and Y. Gao, Appl. Surf. Sci., 2017, 416, 696-703.
- 45 H. Kobayashi, N. Kobayashi, S. Hosoi, N. Koshitani, D. Murakami, R. Shirasawa, Y. Kudo, D. Hobara, Y. Tokita and M. Itabashi, J. Chem. Phys., 2013, 139, 014707.
- 46 W. Chen, H. Huang, S. Chen, X. Gao and T. S. W. Andrew, J. Phys. Chem. C, 2008, 112, 5037.
- 47 S. Duhm, G. Heimel, I. Salzmann, H. Glowatzki, R. L. Johnson, A. Vollmer, J. P. Rabe and N. Koch, Nat. Mater., 2008, 7, 326-332.
- 48 M. Zhu, L. Lyu, D. Niu, H. Zhang, Y. Zhang, P. Liu and Y. Gao, Appl. Surf. Sci., 2017, 402, 142-146.
- 49 H. Xie, D. Niu, Y. Zhao, S. Wang, B. Liu, Y. Liu, H. Huang, P. Wang, D. Wu and Y. Gao, Synth. Met., 2020, 260, 116261.
- 50 R. W. Lof, M. A. van Veenendaal, B. Koopmans, H. T. Jonkman and G. A. Sawatzky, Phys. Rev. Lett., 1992, 68, 3924-3927.
- 51 C. Wang, D. Niu, S. Wang, Y. Zhao, W. Tan, L. Li, H. Huang, H. Xie, Y. Deng and Y. Gao, J. Phys. Chem. Lett., 2018, 9, 5254-5261.
- 52 M. Gobbi, L. Pietrobon, A. Atxabal, A. Bedoya-Pinto, X. Sun, F. Golmar, R. Llopis, F. Casanova and L. E. Hueso, Nat. Commun., 2014, 5, 4161.
- 53 S. Hietzschold, S. Hillebrandt, F. Ullrich, J. Bombsch, V. Rohnacher, S. Ma, W. Liu, A. Kohn, W. Jaegermann, A. Pucci, W. Kowalsky, E. Mankel, S. Beck and R. Lovrincic, ACS Appl. Mater. Interfaces, 2017, 9, 39821-39829.